Miniaturized video-rate epi-third-harmonic-generation fiber-microscope

Shih-Hsuan Chia,[1] Che-Hang Yu,[1] Chih-Han Lin,[1] Nai-Chia Cheng,[1] Tzu-Ming Liu,[2] Ming-Che Chan,[1] I-Hsiu Chen,[1] and Chi-Kuang Sun[1,3*]

[1]*Graduate Inst. of Photonics and Optoelectronics and Department of Electrical Engineering, Natl. Taiwan Univ., Taipei 10617, Taiwan*
[2]*Inst. of Biomedical Engineering, Natl. Taiwan Univ., Taipei 10617, Taiwan*
[3]*Research Center for Applied Sciences, Academia Sinica, Taipei 115, Taiwan*
[*]sun@cc.ee.ntu.edu.tw

Abstract: With a micro-electro-mechanical system (MEMS) mirror, we successfully developed a miniaturized epi-third-harmonic-generation (epi-THG) fiber-microscope with a video frame rate (31Hz), which was designed for in vivo optical biopsy of human skin. With a large-mode-area (LMA) photonic crystal fiber (PCF) and a regular microscopic objective, the nonlinear distortion of the ultrafast pulses delivery could be much reduced while still achieving a 0.4μm lateral resolution for epi-THG signals. In vivo real time virtual biopsy of the Asian skin with a video rate (31Hz) and a sub-micron resolution was obtained. The result indicates that this miniaturized system was compact enough for the least invasive hand-held clinical use.

OCIS codes: (180.4315) Nonlinear microscopy; (190.2620) Harmonic generation and mixing.

References and links

1. http://www.imaginis.com/biopsy/biopsy_risks.asp
2. D. Yelin, and Y. Silberberg, "Laser scanning third-harmonic-generation microscopy in biology," Opt. Express **5**(8), 169–175 (1999).
3. C.-K. Sun, "Higher harmonic generation microscopy," Adv. Biochem. Engin, Biotechnol. **95**, 17–56 (2005).
4. P. J. Campagnola, and L. M. Loew, "Second-harmonic imaging microscopy for visualizing biomolecular arrays in cells, tissues and organisms," Nat. Biotechnol. **21**(11), 1356–1360 (2003).
5. T.-H. Tsai, S.-P. Tai, W.-J. Lee, H.-Y. Huang, Y.-H. Liao, and C.-K. Sun, "Optical signal degradation study in fixed human skin using confocal microscopy and higher-harmonic optical microscopy," Opt. Express **14**(2), 749–758 (2006).
6. S.-Y. Chen, H.-Y. Wu, and C.-K. Sun, "*In vivo* harmonic generation biopsy of human skin," J. Biomed. Opt. **14**(6), 060505 (2009).
7. S.-Y. Chen, S.-U. Chen, H.-Y. Wu, W.-J. Lee, Y.-H. Liao, and C.-K. Sun, "In vivo virtual biopsy of human skin by using noninvasive higher harmonic generation microscopy," IEEE J. Sel. Top. Quantum Electron. **16**, 478–492 (2010).
8. C.-S. Hsieh, S.-U. Chen, Y.-W. Lee, Y.-S. Yang, and C.-K. Sun, "Higher harmonic generation microscopy of in vitro cultured mammal oocytes and embryos," Opt. Express **16**(15), 11574–11588 (2008).
9. S.-P. Tai, W.-J. Lee, D.-B. Shieh, P.-C. Wu, H.-Y. Huang, C.-H. Yu, and C.-K. Sun, "*In vivo* optical biopsy of hamster oral cavity with epi-third-harmonic-generation microscopy," Opt. Express **14**(13), 6178–6187 (2006).
10. M.-R. Tsai, S.-Y. Chen, D.-B. Shieh, P.-J. Lou, and C.-K. Sun, "*In vivo* optical virtual biopsy of human oral cavity with harmonic generation microscopy," Proc. SPIE (to be published).
11. C.-K. Sun, C.-C. Chen, S.-W. Chu, T.-H. Tsai, Y.-C. Chen, and B.-L. Lin, "Multiharmonic-generation biopsy of skin," Opt. Lett. **28**(24), 2488–2490 (2003).
12. S.-P. Tai, T.-H. Tsai, W.-J. Lee, D.-B. Shieh, Y.-H. Liao, H.-Y. Huang, K. Zhang, H.-L. Liu, and C.-K. Sun, "Optical biopsy of fixed human skin with backward-collected optical harmonics signals," Opt. Express **13**(20), 8231–8242 (2005).
13. J.-H. Lee, S.-Y. Chen, C.-H. Yu, S.-W. Chu, L.-F. Wang, C. K. Sun, and B. L. Chiang, "Noninvasive in vitro and in vivo assessment of epidermal hyperkeratosis and dermal fibrosis in atopic dermatitis," J. Biomed. Opt. **14**(1), 014008 (2009).
14. T. Yasui, Y. Takahashi, M. Ito, S. Fukushima, and T. Araki, "*Ex vivo* and *in vivo* second-harmonic-generation imaging of dermal collagen fiber in skin: comparison of imaging characteristics between mode-locked Cr:forsterite and Ti:sapphire lasers," Appl. Opt. **48**(10), D88–D95 (2009).
15. L. Fu, A. Jain, H. Xie, C. Cranfield, and M. Gu, "Nonlinear optical endoscopy based on a double-clad photonic crystal fiber and a MEMS mirror," Opt. Express **14**(3), 1027–1032 (2006).

16. W. Piyawattanametha, R. P. J. Barretto, T. H. Ko, B. A. Flusberg, E. D. Cocker, H. Ra, D. Lee, O. Solgaard, and M. J. Schnitzer, "Fast-scanning two-photon fluorescence imaging based on a microelectromechanical systems two- dimensional scanning mirror," Opt. Lett. **31**(13), 2018–2020 (2006).

17. H. J. Shin, M. C. Pierce, D. Lee, H. Ra, O. Solgaard, and R. Richards-Kortum, "Fiber-optic confocal microscope using a MEMS scanner and miniature objective lens," Opt. Express **15**(15), 9113–9122 (2007).

18. W. Piyawattanametha, E. D. Cocker, L. D. Burns, R. P. J. Barretto, J. C. Jung, H. Ra, O. Solgaard, and M. J. Schnitzer, "*In vivo* brain imaging using a portable 2.9 g two-photon microscope based on a microelectromechanical systems scanning mirror," Opt. Lett. **34**(15), 2309–2311 (2009).

19. T.-M. Liu, M.-C. Chan, I.-H. Chen, S.-H. Chia, and C.-K. Sun, "Miniaturized multiphoton microscope with a 24Hz frame-rate," Opt. Express **16**(14), 10501–10506 (2008).

20. C. L. Hoy, N. J. Durr, P. Chen, W. Piyawattanametha, H. Ra, O. Solgaard, and A. Ben-Yakar, "Miniaturized probe for femtosecond laser microsurgery and two-photon imaging," Opt. Express **16**(13), 9996–10005 (2008).

21. B. A. Flusberg, J. C. Jung, E. D. Cocker, E. P. Anderson, and M. J. Schnitzer, "*In vivo* brain imaging using a portable 3.9 gram two-photon fluorescence microscope," Opt. Lett. **30**(17), 2272–2274 (2005).

22. R. Le Harzic, M. Weinigel, I. Riemann, K. König, and B. Messerschmidt, "Nonlinear optical endoscope based on a compact two axes piezo scanner and a miniature objective lens," Opt. Express **16**(25), 20588–20596 (2008).

23. R. Le Harzic, I. Riemann, M. Weinigel, K. König, and B. Messerschmidt, "Rigid and high-numerical-aperture two-photon fluorescence endoscope," Appl. Opt. **48**(18), 3396–3400 (2009).

24. Y. Wu, Y. Leng, J. Xi, and X. Li, "Scanning all-fiber-optic endomicroscopy system for 3D nonlinear optical imaging of biological tissues," Opt. Express **17**, 7901–7915 (2009).

25. C. J. Engelbrecht, R. S. Johnston, E. J. Seibel, and F. Helmchen, "Ultra-compact fiber-optic two-photon microscope for functional fluorescence imaging *in vivo*," Opt. Express **16**(8), 5556–5564 (2008).

26. J. Sawinski, and W. Denk, "Miniature random-access fiber scanner for *in vivo* multiphoton imaging," J. Appl. Phys. **102**(3), 034701 (2007).

27. J. C. Jung, and M. J. Schnitzer, "Multiphoton endoscopy," Opt. Lett. **28**(11), 902–904 (2003).

28. D. Bird, and M. Gu, "Two-photon fluorescence endoscopy with a micro-optic scanning head," Opt. Lett. **28**(17), 1552–1554 (2003).

29. M. J. Levene, D. A. Dombeck, K. A. Kasischke, R. P. Molloy, and W. W. Webb, "*In vivo* multiphoton microscopy of deep brain tissue," J. Neurophysiol. **91**(4), 1908–1912 (2004).

30. W. Göbel, J. N. D. Kerr, A. Nimmerjahn, and F. Helmchen, "Miniaturized two-photon microscope based on a flexible coherent fiber bundle and a gradient-index lens objective," Opt. Lett. **29**(21), 2521–2523 (2004).

31. H. Bao, and M. Gu, "A 0.4-mm-diameter probe for nonlinear optical imaging," Opt. Express **17**(12), 10098–10104 (2009).

32. D. Kobat, M. E. Durst, N. Nishimura, A. W. Wong, C. B. Schaffer, and C. Xu, "Deep tissue multiphoton microscopy using longer wavelength excitation," Opt. Express **17**(16), 13354–13364 (2009).

33. I.-H. Chen, S.-W. Chu, C.-K. Sun, P.-C. Cheng, and B.-L. Lin, "Wavelength dependent cell damages in multi-photon confocal microscopy," Opt. Quantum Electron. **34**(12), 1251–1266 (2002).

34. K. König, P. T. C. So, W. W. Mantulin, and E. Gratton, "Cellular response to near-infrared femtosecond laser pulses in two-photon microscopes," Opt. Lett. **22**(2), 135–136 (1997).

35. P.-C. Cheng, B.-L. Lin, F.-J. Kao, M. Gu, M.-G. Xu, X. Gan, M.-K. Huang, and Y.-S. Wang, "Multi-photon fluorescence microscopy--the response of plant cells to high intensity illumination," Micron **32**(7), 661–669 (2001).

36. M.-C. Chan, T.-M. Liu, S.-P. Tai, and C.-K. Sun, "Compact fiber-delivered Cr:forsterite laser for nonlinear light microscopy," J. Biomed. Opt. **10**(5), 054006 (2005).

37. J. Schutz, W. Hodel, and H. Weber, "Nonlinear pulse distortion at the zero dispersion wavelength of an optical fibre," Opt. Commun. **95**(4-6), 357–365 (1993).

38. V. P. Yanovsky, and F. W. Wise, "Nonlinear propagation of high-power, sub-100-fs pulses near the zero-dispersion wavelength of an optical fiber," Opt. Lett. **19**(19), 1547–1549 (1994).

39. K. G. Jespersen, T. Le, L. Grüner-Nielsen, D. Jakobsen, M. E. V. Pederesen, M. B. Smedemand, S. R. Keiding, and B. Palsdottir, "A higher-order-mode fiber delivery for Ti:Sapphire femtosecond lasers," Opt. Express **18**(8), 7798–7806 (2010).

40. C. K. Sun, C. H. Yu, S. P. Tai, C. T. Kung, I. J. Wang, H. C. Yu, H. J. Huang, W. J. Lee, and Y. F. Chan, "*In vivo* and *ex vivo* imaging of intra-tissue elastic fibers using third-harmonic-generation microscopy," Opt. Express **15**(18), 11167–11177 (2007).

41. C.-H. Yu, S.-P. Tai, C.-T. Kung, W.-J. Lee, Y.-F. Chan, H.-L. Liu, J.-Y. Lyu, and C.-K. Sun, "Molecular third-harmonic-generation microscopy through resonance enhancement with absorbing dye," Opt. Lett. **33**(4), 387–389 (2008).

42. C.-F. Chang, H.-C. Chen, M.-J. Chen, W.-R. Liu, W.-F. Hsieh, C.-H. Hsu, C.-Y. Chen, F.-H. Chang, C.-H. Yu, and C.-K. Sun, "Direct backward third-harmonic generation in nanostructures," Opt. Express **18**(7), 7397–7406 (2010).

43. C.-F. Chang, C.-Y. Chen, F.-H. Chang, S.-P. Tai, C.-Y. Chen, C.-H. Yu, Y.-B. Tseng, T.-H. Tsai, I.-S. Liu, W.-F. Su, and C.-K. Sun, "Cell tracking and detection of molecular expression in live cells using lipid-enclosed CdSe quantum dots as contrast agents for epi-third harmonic generation microscopy," Opt. Express **16**(13), 9534–9548 (2008).

44. C.-F. Chang, C.-H. Yu, and C.-K. Sun, "Multi-photon resonance enhancement of third harmonic generation in human oxyhemoglobin and deoxyhemoglobin," to be published in J. Biophoton. (2010).

1. Introduction

The mortality from malignancies is still high despite many efforts in the past. Definitive diagnosis in the early stage is thus vital for improving the quality of life since malignancies are more probably curable in this stage. Physical biopsy which could provide a sub-micron lateral resolution for the pathohistological diagnosis was regarded as the gold-standard for early diagnosis. However, the invasive sampling of physical biopsy takes risks of trauma, infection, hematoma, and hemorrhage [1]. Moreover, using this centuries-old approach, we are disabled to study living bio-activities since the sampled tissue is no longer alive. Thus, in order to make a definitive diagnosis in the early stage, the least invasive *in vivo* microscopic technique that keeps the advantages of physical biopsy is highly required.

Recently, the optical harmonics signature, including both second harmonic generation (SHG) and THG, of the tissue offers new horizons for biomedical imaging [2–13]. Comparing with confocal microscopy, due to the characteristic of optical nonlinearity, harmonic generation microscopy could provide better optical sectioning capability without the need of confocal pinhole [2–5]. In addition, because of the nature of energy conservation of harmonic generation (HG) process, HG leaves no energy deposition to the interacted specimens and thus can be considered as a truly noninvasive modality in contrast with other electron-transition based nonlinear processes [2–4]. In previous clinical observations, epi-THG microscopy was found to provide *in vivo* morphological images with detailed histological information including sizes, shapes, and distributions of basal cells, as well as with a high penetrability of ~300µm, a sub-µm spatial resolution, while no photodamages were reported [6–8]. Besides, the movement of red blood cells in capillaries can also be clearly resolved *in vivo* by epi-THG microscopy without the need of fluorescent labeling [6,7,9]. Epi-harmonic generation microscopy (epi-HGM) has thus emerged as a promising microscopic technique for optical virtual biopsy [6,7,9–14].

For further clinical *in vivo* observation of human tissues, extending this nonlinear optical imaging technique for hand-held or endoscopic applications is necessary. The imaging system should be miniaturized as a flexible, compact, and easily-used one instead of using complicated bulk optics. In addition, high frame rate acquisition is also an important issue for submicron resolution imaging: it is hard to prevent the slight movements, which could emanate from heart beats and breathing; on the other hand, it is important to observe the fast physiological processes such as blood flow.

Many research groups have focused on developing miniature laser-scanning probes [15–31]. In general, the major challenges of the miniaturization were divided into two parts: one is the scanning unit and the other is the miniaturized probe, including relay lenses and objectives. To reduce size for potential applications, several scanner configurations have been commonly developed by using MEMS mirrors [15–20] or fiber cantilevers [21–26]. The size reduction of the miniaturized probes usually employed a gradient-index (GRIN) rod lens [15,20,21,23–25,27–29]. Two-photon fluorescence (2PF) endoscopy was studied previously and it has been applied to in vivo animal observation [18,21,25,26,29]. Although the compact size could be achieved by using a GRIN rod, the low numerical aperture (NA) of the rod, typically smaller than 0.65 [23], limited not only the excitation efficiency but also the imaging resolution. Furthermore, commonly using femtosecond Ti:sapphire laser as an excitation source cannot provide the capability of both THG imaging and superior depth penetration [3,14,32]. In a previous work, we have also demonstrated a miniaturized probe for 2PF microscopy with a high frame rate [19]. However, the previous achievement cannot obtain nonlinear light images, especially THG images, with a video rate and a backward epi-detection scheme. The light delivery is also not fiber-based., The further advancements in the optical design, the higher-speed scanning system, and fiber-delivery are necessary for future biomedical and clinical applications, especially for noninvasive in vivo THG microscopic imaging. In this work, a compact THG fiber-microscope with a compact size, sub-micron resolution, and a video rate is demonstrated, and has been applied for in vivo virtual harmonics biopsy of the human skin.

2. Video-rate fiber-microscopic system and experimental methods

2.1 Miniature high-speed scanning probe

2.1.1 MEMS scanning scheme

Recent technical advancement of the two-dimensional (2D) scanning MEMS mirror increased the resonant frequency of the mirror up to several KHz on both axes [19]. High frame rate could thus be achieved by using high-resonant-frequency MEMS mirrors. We employed a 2D-scanning MEMS mirror (PE100011, OPUS Microsystems corp., Taiwan) which was resonantly scanning at frequencies of fx=16.41 kHz and fy=1.71 kHz. The line scanning rate was even higher than a previous work [19]. When 0~70V square waves were applied to the mirror, the incident laser beam was sinusoidally deflected by 19 degrees in the x axis, the fast axis, and by 15 degrees in the y axis, the slow axis.

The scanning mechanism and the image reconstruction are similar to a previous work [19]. The scanning area on the focal plane was reconstructed to a 512×512-pixel image. To scan through all the pixels, the frame trigger, which was used to initiate the data acquisition, was set as 15.53 Hz. Because the scanning frequency of the fast axis was only ten times the frequency of the slow one's, the laser beam didn't scan line-by-line on the focal plane of the objective lens: before it scanned through a line in the x direction, the trajectory of the laser beam had moved to another line in the y direction of the 512×512-pixel image. Therefore, unlike the raster scanning method, the frame rate of the Lissajous trace was not equal to the frequency of the frame trigger. That is, the initial pixel of each frame was not necessary at the same position of the focal plane of the objective. Thus, the frame rate could be set arbitrarily as long as the number of the missing points in a frame was tolerable. The detected analog voltage signals were sampled by a data acquisition card (PCI-5105, National Instruments) with an external sampling clock, 36.111 MHz. By using a Field Programmable Gate Array (FPGA) card, all the electronic signals were synchronized, divided by a generated clock with a frequency of 108.333MHz. The FPGA board was used to generate four synchronized control signals: the driving signals for the both axes of the MEMS mirror, a frame trigger, and a sampling clock. The driving signals were amplified and then resonantly drove the MEMS mirror without the need of the feedback control. The frame trigger and the sampling clock were sent to the data acquisition card for the imaging acquisition. The counts of sampling points per pixel in a frame trigger period are shown in Fig. 1. Due to the nature of sinusoidal scanning, the pixels around the edge of the image were passed much more times than those close to the center. If the illuminating power is below the damage threshold, this characteristic improves the SN ratio around the edge. In addition, the sampling clock was high enough that we could divide one frame trigger period into two frames. A frame rate as high as 31 Hz was thus achieved.
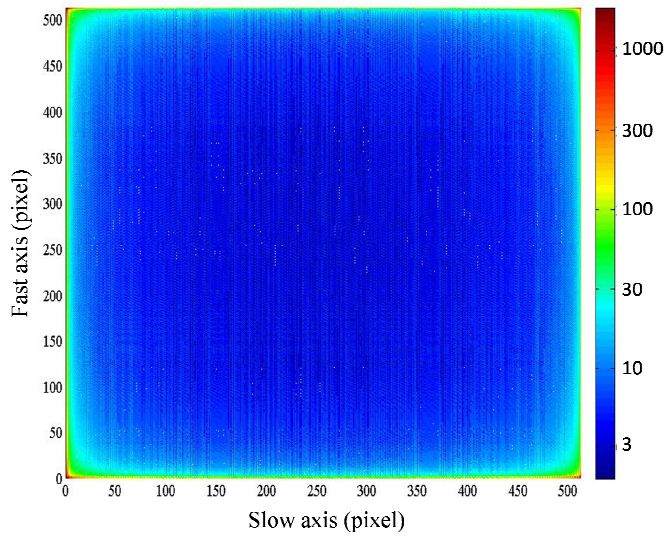
Fig. 1. The counts of sampling points per pixel in a frame trigger period.

Since the scanning frequency of the fast axis (>16 KHz) was much higher than the typical one in the raster scanning method, the imaging resolution might be hampered not only by the optical limit, but also by the maximum distance of the adjacent sampling points on the imaging plane. The maximum distance, d_{max}, could be roughly estimated as

$$d_{max} \sim \frac{\pi[(f_x l_x)^2 + (f_y l_y)^2]^{1/2}}{f_{sampling}},$$ (1)

where l_x and l_y are the imaging sizes of the two axes on the imaging plane, and $f_{sampling}$ is the sampling frequency. In this reported case, the imaging size (the x axis by the y axis) was 100μm×70μm. The display resolution of the imaging was limited by ~140nm of the maximum distance, which is much smaller than the optical resolution.

2.1.2 Relay lens design

To miniaturize the system without sacrificing the spatial resolution for sub-cellular imaging purpose, an aberration-reduced miniaturized probe with a high NA is required. Instead of using a GRIN rod, we simply employed a pair of miniaturized spherical relay lenses, and still used a commercial objective to achieve the sub-micron spatial resolution. The relay lenses were used to image the laser spot on the MEMS mirror into the back aperture of the objective. When the MEMS mirror scanned, the deflected laser beam was expanded to fit the back aperture of the objective by the relay lenses. Then, the deflected beam was focused by the objective and scanned on the focal plane. To obtain a sub-micron spatial resolution, the spherical aberration and coma induced by oblique incidence should be reduced. The ZEMAX software was used to design and to simulate the radius of curvature (ROC) of the custom lenses. The first designed lens was made of SF11 glass with 9.98mm ROC on the incident side and -7.97mm ROC on the other side. The second lens was made of BK7 with 80.03mm ROC on the incident side and -56.82mm ROC on the other side. The effective focal length of the first lens and second lens were 5mm and 65mm, respectively. Both lenses have a 10mm diameter and a 7mm thickness. For simulating the result, we combined a 60X water immersion objective and treating it as a perfect lens with a 3mm focal length. The entrance pupil of the system was 0.6mm in diameter and the designed maximum scanning angle was ± 10 degree. Figure 2 shows the optical path differences of the designed system. The designed

result indicated that the maximum wavefront difference of the designed system was smaller than λ/4, so that the image resolution and quality won't be affected much by the oblique incidence. In addition, the focal length difference at the imaging plane was smaller than 1µm.
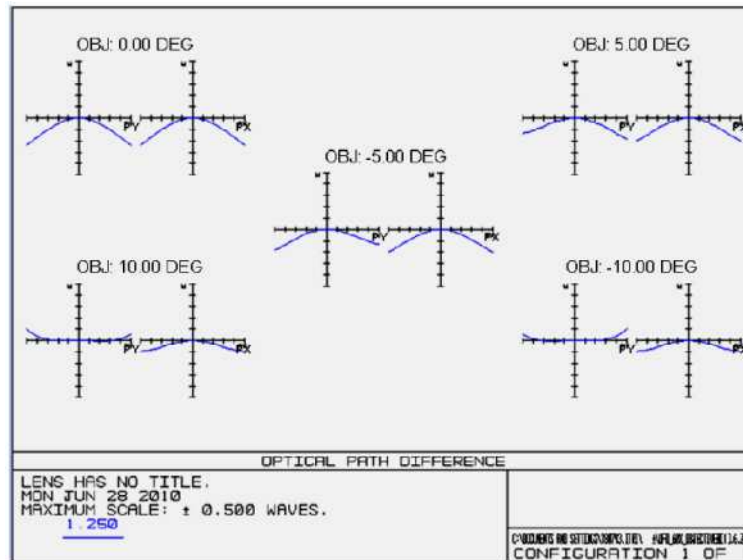

Fig. 2. The optical path differences of the designed result.

2.2 Fiber delivery of femtosecond light source

Instead of using commonly-used Ti:sapphire lasers, we employed a home-made femtosecond Cr:forsterite laser with a 85MHz repetition rate as an excitation source. The operating window of the laser was falling in the 1.2 µm ~1.3 µm regime. A Cr:forsterite-based system can acquire sectioned images with a deeper penetration depth and with much reduced photodamage than using a Ti:sapphire laser [3,14,32–35]. In addition, the corresponding SHG and THG signals fall in the visible regime, making them compatible to most microscope optics and objectives [3]. Furthermore, since the operating window was close to the zero dispersion wavelength of the common silica fiber, the dispersion effect is strongly reduced and it makes fiber-based nonlinear light microscopy possible without extra dispersion compensation unit [36].

Without the use of pre-chirping units, we used a LMA PCF with a 35µm core size and chose a suitable fiber length for the delivery of femtosecond laser pulses. The photonic structures maintained single-mode operation even though the core size was much larger than common single-mode fibers. The mode field diameter of the fiber is 26 µm. We coupled the laser into a piece of 12 cm nonlinear photonic crystal fiber (LMA 35, Crystal Fibre A/S) with a 60% coupling efficiency.

The results are shown in Fig. 3. The spectrum and the pulse width were slightly broadened by self-phase modulation and higher-order dispersion when the fiber-output power was as high as 422 mW [37,38]. Figure 3(a) shows that the corresponding output bandwidth was 57 nm. The full width at the half maxima (FWHM) of the autocorrelation trace was 140 fs, corresponding to 100fs FWHM pulse width by assuming a Gaussian pulse shape, as shown in Fig. 3(b). For future endoscopic and handheld applications, longer fiber length will be desired. Longer fiber length could be achieved by using a hollow core PCF designed at the demonstrated operating wavelength (1250 nm) to reduce both the temporal distortion and optical nonlinear effect or by using a higher-order-mode fiber delivery [39].
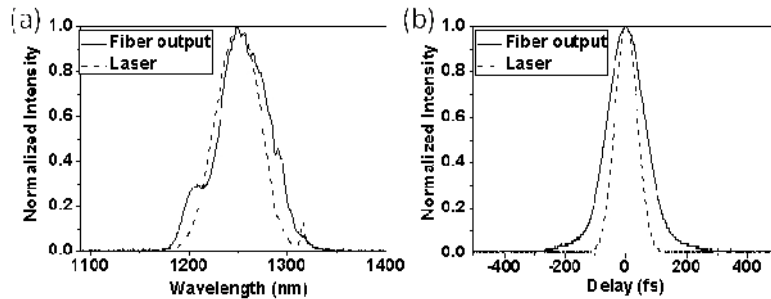
Fig. 3. (a) The spectra and (b) the autocorrelation traces of the Cr:forsterite laser (the dotted lines) and the fiber-based femtosecond source (the solid lines).

3. Experimental setup

The experimental setup is illustrated in Fig. 4. We combined the fiber-based light source, the MEMS mirror, and the miniaturized probe. The reflecting area of the MEMS mirror was a silicon plate suspended by two torsional springs. Gimbal mounting of the mirror plate was used and the reflectivity of the mirror plate was enhanced by a thin layer of aluminum. The reflectivity of the mirror was ~82%. For high transmission of the incident and reflected laser beams, the protecting glass window covering the MEMS mirror and the relay lenses were anti-reflection coated around the wavelength of 1250 nm. After the MEMS mirror and the designed relay-lens set, a dichroic mirror (T1070SP_XXT, Chroma) was placed to reflect the scanning laser beam, and the scanning beam was focused on the sample by a 1.2NA 60X water immersion objective (UPlanApo60XW/IR, Olympus).

As the skin or the sample moved to the focal plane, the generated SHG and THG signals were epi-collected in a reflection geometry by using the same objective, then coupled into a multimode fiber (FT800EMT, Thorlabs), and then guided to the detecting unit. Because the outer diameter of the whole module (including the mounting) was designed to be within 3cm, this system was compact enough for *in vivo* hand-held human skin observation.
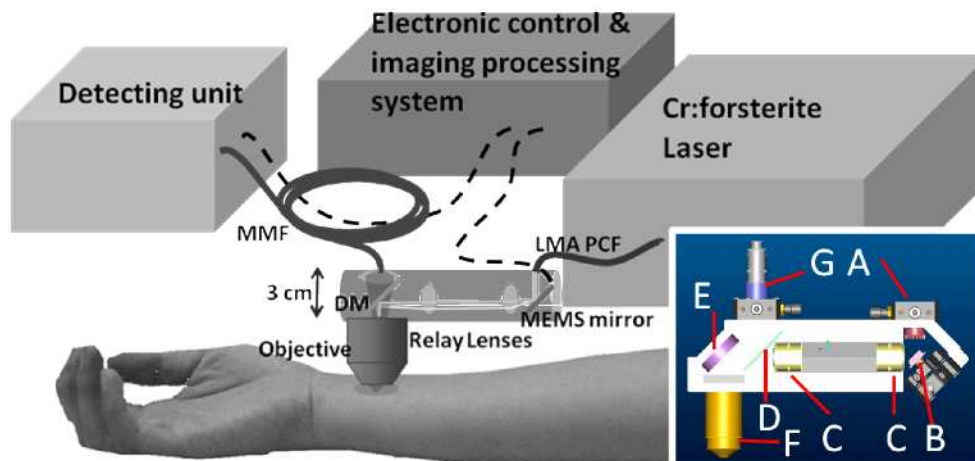

Fig. 4. The schematic diagram of the miniaturized THG fiber-microscope. DM: dichroic mirror; MMF: multi-mode fiber; Dot line: electronic line. The inset shows the detailed schematic layout of the designed microscope. A: LMA PCF collimator; B: MEMS mirror; C: relay lenses; D: dichroic mirror; E: broadband mirror; F: objective; G: MMF coupler.

At the detection side, we divided the output of the collection multimode fiber into the THG and SHG channels by a dichroic mirror (440DCLP, Chroma), and the HG signals were detected by two separate thermal electric (TE)-cooled photomultiplier tubes (PMTs) with 410nm and 615nm filters. The detected electrical signals were sent to a computer for the

imaging construction. The reconstructed images or movies were displayed and saved on the computer.

4. Performance

4.1 The epi-THG image of micro-beads

We first tested the resolution performance of the laser scanning imaging system by observing the moving 1μm-diameter fluorescent beads (F-8816, FluoSpheres) in solution. The epi-THG signals of the beads were enhanced by resonant enhancement since the absorption peak of the beads was at 620 nm, which was close to two-photon wavelength [40,41]. The detected epi-THG signals could originate from both forward-scattered emission and backward-directed generation [42,43]. Unlike fluorescence, the emitted pattern of the coherent THG process is related to the coherence length, the optimized interaction length within which the coherent addition of the signal field is constructive. When the sphere's diameter exceeds the coherence length, the phase mismatch causes destructive interference of the THG radiation from the various parts of the sample. In regard of the forward THG emission under the tight focusing condition, the coherence length, ~1μm, is dominant by the Gouy phase shift. On the other hand, the coherent length of the backward-directed THG, ~87 nm in this case [43], was mainly decided by the refractive index of the sample. The corresponding refractive indices of the polystyrene beads with respect to water were 1.19 at 1250 nm and 1.20 at 415 nm. Thus, if the forward-scattered-THG signals were mainly detected in the imaging, the 1μm-diameter beads appeared as a solid circular plate and the maximum intensity of THG signals was at the center of the beads. Otherwise, the maximum intensity of epi-THG was expected to be observed near where the thickness of the beads was around 87 nm.

To further analyze the emission pattern, we randomly picked 4 beads and averaged their images with a magnified field-of-view. The averaged image is shown in Fig. 5(a). The location and the existence of the bead were double-checked by overlapping the 2PF images (red).
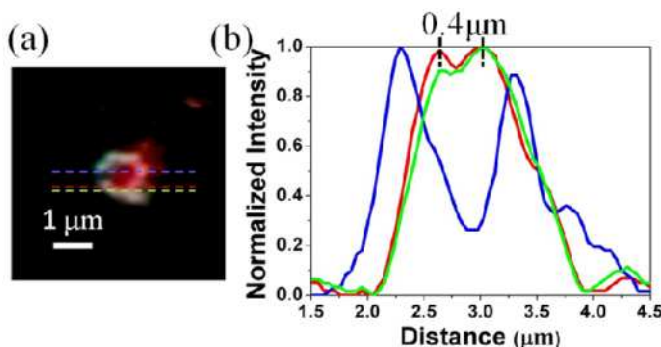

Fig. 5. (a) The averaged image of the 1μm fluorescent beads. Red: 2PF; White: THG. (b) Intensity distributive THG profiles of (a) along the center of the bead (blue), along the red line, where the THG pattern of the bead was just resolved (red), and along the green line, where the THG pattern could not be resolved (green).

Since the THG imaging of the bead appeared as a circle, the detected THG signals were mainly contributed from the backward-directed THG. In Fig. 5(b), the minimum distance of which the separated THG signals could be resolved (the red line) was ~0.4 μm. Thus, a 0.4μm transverse resolution of the backward-directed THG emission was obtained with our laser-scanning miniaturized system.

4.2 In vivo optical harmonics biopsy of human skin

To testify the applicability to the clinical observation, we further applied the miniaturized THG fiber-microscope for *in vivo* trial on human skin. The optical harmonics biopsy was performed on the ventral forearm skin of an Asian woman. The experimental protocol of the

clinical trial followed the previous works [6,7] and it was approved by the institutional review board (IRB) of National Taiwan University Hospital. The average illuminating power into the skin of the volunteer was about 108 mW and the exposure time in one area was less than 30 minutes. No stinging sensation was reported by the volunteer and no pathological change was evaluated by a dermatologist.
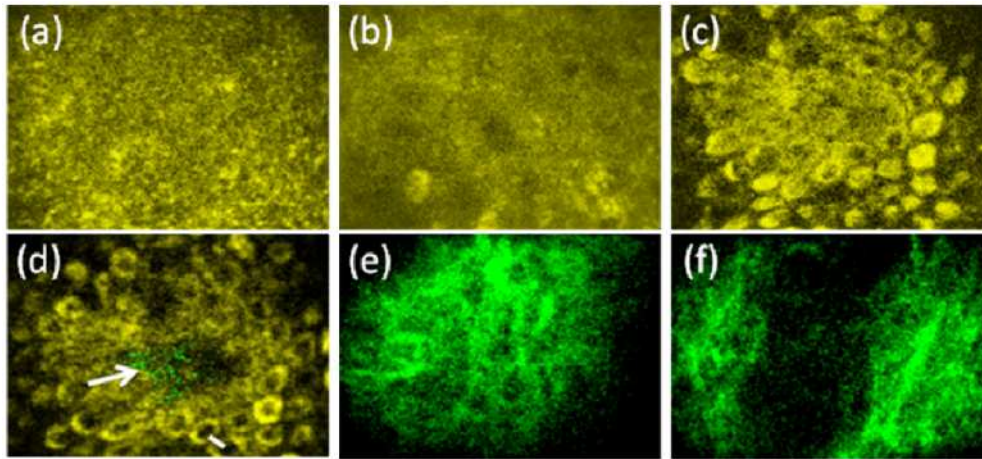

Fig. 6. *In vivo* horizontal-sectioned epi-THG and epi-SHG images of Asian forearm skin in different layers. In the epidermis, the morphology of (a) the *stratum corneum*, (b) the *stratum spinosum*, (c) the upper section and (d) the deeper section of the *stratum basale* (Media 1) could all be clearly distinguished using this epi-THG fiber-microscopy. Combined with the epi-SHG modality, the collagen fibers in the dermal papilla [arrowhead in (d)] were revealed; (e) and (f) the collagenous distribution in the dermis was also observed through epi-SHG. Yellow: THG; Green: SHG. Image size: 100μm×70μm. The integration time of each image except (b) is 0.33 second and 2 second in (b).

Figure 6 shows the acquired *in vivo* HG biopsy images from epidermis to dermis. The 512×512-pixel image sizes in both Fig. 6 and Fig. 7 were rescaled to fit the actual ratio of the scanning area, 100μm×70μm. In *in vivo* skin observation, THG imaging contrasts were found to be dominated by the interfaces [3,6] between lipid and corneocytes and the cytoplasmic organelles [6,8]. By epi-THG microscopy, the cell morphology of different layers in the epidermis could be clearly distinguished through the THG-bright cytoplasm. By analyzing the THG profile (not shown) along the white line crossing the adjacent cells in Fig. 6(d), the result indicated that the fine structure smaller than 1μm was easily resolved even near the boundary of the image. Besides, the recorded movie in Fig. 6(d) also shows that it is hard to prevent vibrations from the volunteer. In the dermis, the epi-SHG signature revealed the distinct collagenous structures. The FWHM of the fitting Gaussian curve (not shown) of the thinnest fiber in Fig. 6(f) was 0.7 μm, indicating the sub-micron resolution capability for SHG even deep inside the dermis layer. Greater-than-200μm penetrative ability was achieved in the clinical trial.
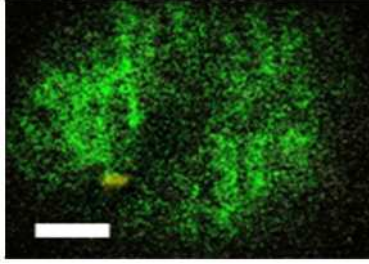
Fig. 7. The five times slower movie showing the *in vivo* blood flow with a speed of ~300 µm/s (Media 2). Yellow: THG; Green: SHG. Image size: 100µm×70µm. Scale bar: 20 µm. Actual size of the recorded movie: 512×512 pixels

In addition, because the resonance behavior of oxy-hemoglobin transition enhances the epi-THG contrast of the erythrocytes in the capillary [44], this makes the *in vivo* observation of the blood flow deep inside the dermis possible [6]. Figure 7 shows the five times slower repeated movie of the observed blood flow in the dermis. This movie was acquired by the developed fiber-microscope with a 31 frame/s rate. To reduce the noise under such a high frame rate, the THG signals in the capillary were Gaussian blurred and a single red blood cell can be distinguished in the movie. The blood flow with a speed as fast as ~300 µm/s in the capillary was visualized.

5. Summary

To our best knowledge, the first-ever miniaturized epi-THG fiber-microscope with a sub-micron spatial resolution and a video frame rate was demonstrated for in vivo optical harmonics biopsy. By choosing a suitable fiber length, the nonlinear distortion of the fiber delivery was much reduced. We successfully delivered a ~100fs excitation pulse with a ~5nJ pulse energy. Using optical nonlinearity in tissue, the THG transverse resolution could be down to 0.4 µm through a regular high NA microscope objective. Video-rate imaging was also obtained at the same time by asynchronous scanning of a MEMS mirror with a 16.4 KHz resonant frequency. The blood flow with a speed of sub-mm per second was successfully observed. Our result suggests that this high-speed MEMS-based system could be applied to observe dynamic biological activities in vivo. Greater than 200µm penetrative depth, sub-micron resolution, and video-rate imaging for optical skin biopsy was simultaneously realized with this compact fiber-microscope.

Acknowledgement